

Supporting Information for “Determining the Structure–Property Relationships of Quasi-Two-Dimensional Semiconductor Nanoplatelets”

Arin R. Greenwood^{*,†} Sergio Mazzotti^{*,‡} David J. Norris[‡] and Giulia Galli^{*,†,¶,§}

[†]*Pritzker School of Molecular Engineering, University of Chicago, Chicago, IL 60637, USA*

[‡]*Optical Materials Engineering Laboratory, Department of Mechanical and Process Engineering, ETH Zurich, Zurich 8092, Switzerland*

[¶]*Department of Chemistry, University of Chicago, Chicago, IL 60637, USA*

[§]*Argonne National Laboratory, Argonne, IL 60439, USA*

E-mail: gagalli@uchicago.edu

S1 Computational details

Structures of 2, 3, 5, and 7ML NPLs capped with Cl^- ligands were generated using 2x2x1 supercells (28-68 atoms) with 3x3x1 k-points, allowing both the in-plane lattice constants and the atom positions to relax until forces were below 10^{-5} a.u. Cl^- ligands were initially placed in a bridging configuration between Cd atoms prior to relaxation, consistent with literature.¹ All calculations were performed with PseudoDojo pseudopotentials,² as we found that the 3d electrons included in the valence for Se were essential to reproduce a band gap in quantitative agreement with experiment. A kinetic energy cutoff of 100 Ry was used for all calculations, with a vacuum spacing of at least 17 Angstrom in the out-of-plane direction to separate periodic replicas.

G_0W_0 and BSE calculations were performed for 2 to 5ML and 2 to 3ML NPLs, respectively. For G_0W_0 (BSE) calculations, a primitive unit cell of 7-13 atoms (7-9 atoms) was used to reduce the number of electrons per calculation. Each primitive unit cell was symmetrized to remove spurious numerical differences in the lattice constants in x and y and reduce the number of k-points needed to explicitly calculate, with a difference in band gap compared to the non-symmetrized structure of less than 0.1 meV.

In contrast to the uniform hydrostatic strain profile present in quantum dots, NPLs are governed by biaxial stress that has a unique effect on both the band gaps and symmetry of the electronic energy levels. We find that the relaxed in-plane lattice constant of each NPL is smaller than the bulk lattice constant; this compression is partially offset by a tensile strain and lattice expansion in the out-of-plane (axial) direction. We note that this effect would not be observed in structural models that allow only the atom positions but not the lattice constants to relax (this is commonly done in literature).

G_0W_0 quasiparticle energies were calculated for the 2ML, 3ML and 5ML NPLs, while BSE calculations were performed on 2ML and 3ML NPLs only. G_0W_0 calculations were performed using the West code,³ which does not require explicit calculation of empty states and avoids inversion of dielectric matrices. G_0W_0 quasiparticle gaps were then extrapolated

to infinite number of k-points in the lateral dimensions and to infinite number of projective dielectric eigenpotentials (PDEPs) to ensure converged results. The long-range Coulomb interaction was truncated to properly converge with respect to vacuum size in the axial direction, using the method discussed in Ref.⁴ For G_0W_0 calculations in West, we found that a sufficiently large k-point mesh of at least $5 \times 5 \times 1$ was essential prior to extrapolation to infinite k-points due to the method used in the code for the Coulomb truncation.

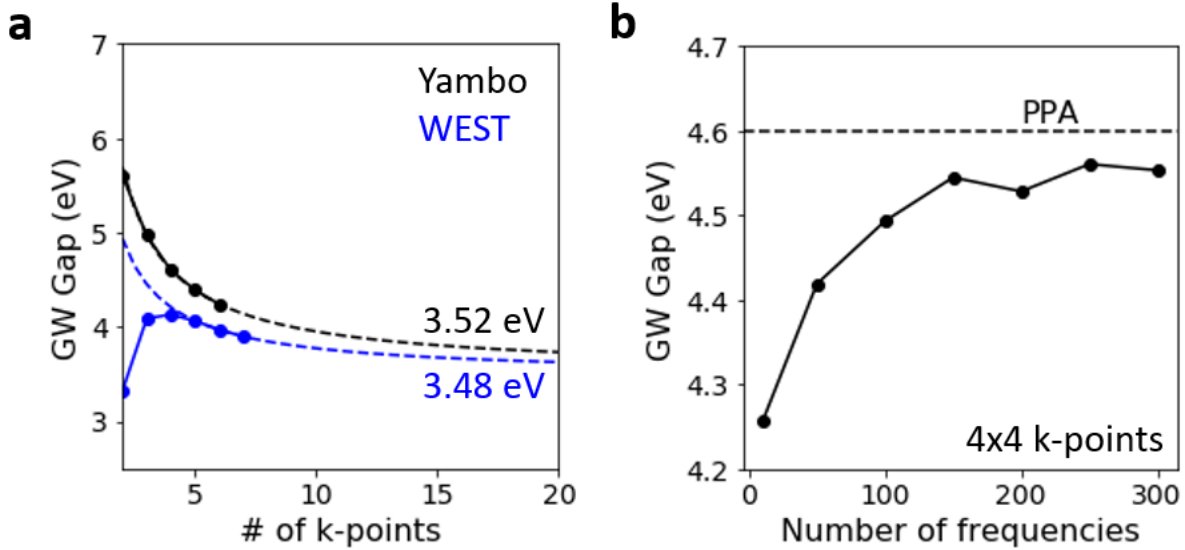


Figure S1: a) Comparison of the convergence of the G_0W_0 band gap with respect to k-point mesh for a 2ML CdSe NPL, obtained using Yambo (PPA) and West (FF), demonstrating that the two codes agree after extrapolating to infinite k-points, but not for small k-point meshes, due to different methods adopted for the truncation of the Coulomb potential. The x axis gives number of k-points in the in-plane direction, i.e. $4 \times 4 \times 1$, etc. b) Comparison of PPA to FF approaches using Yambo with a $4 \times 4 \times 1$ k-point mesh for the 2ML NPL, as a function of increasing number of explicitly calculated frequencies.

For the 2ML NPL, in Fig. S1a we provide a detailed comparison between G_0W_0 calculations using West and the Yambo code,^{5,6} the latter of which uses the Plasmon-Pole Approximation (PPA) of Godby and Needs⁷⁻⁹ rather than the full-frequency (FF) approach of West. Yambo calculations of the quasiparticle gap were conducted with 100 empty states, and the Coulomb interaction was truncated using the Random Integration Method (RIM).¹⁰ We found that, after extrapolating to infinite k-point meshes, quasiparticle gaps calculated

with the two codes converge to within 40 meV (Fig S1a), with the remaining small discrepancy accounted for by the difference between PPA and FF approaches (Fig S1b, where both PPA and FF are calculated with Yambo).

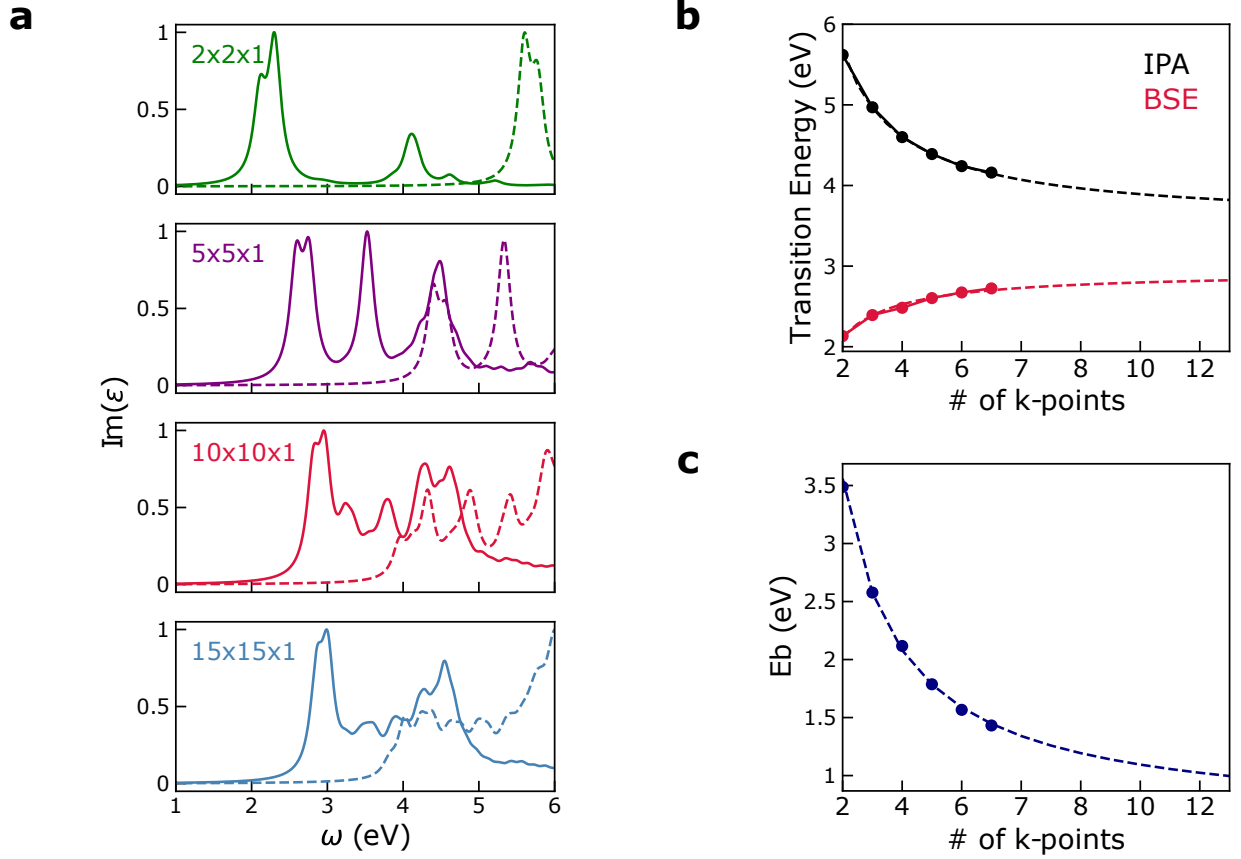


Figure S2: a) Examples of BSE spectra obtained at different k-point densities, from $2 \times 2 \times 1$ to $15 \times 15 \times 1$, for a 2ML CdSe NPL. Solid lines are from BSE, while dashed lines are from the Independent Particle Approximation (IPA). Spectra are plotted with a Lorentzian broadening of 0.1 eV. b) Convergence as a function of k-points of the first transition energy for the IPA spectrum (black, same as HOMO-LUMO G_0W_0 gap) and BSE (red). c) Convergence as a function of k-points of the exciton binding energy of the 2ML NPL, calculated as the difference between the first transition energies of IPA and BSE.

The exciton binding energy and absorption spectra of CdSe NPLs were calculated through the Bethe-Salpeter Equation (BSE) using the Yambo code^{5,6} and using PBE wavefunctions and a scissor correction equal to the difference between the G_0W_0 and PBE gaps at the chosen k-point density for the 2ML and 3ML NPLs. The final spectrum for the 2ML NPL was calculated with a $15 \times 15 \times 1$ k-point mesh, while exciton binding energies for the larger

NPLs were extrapolated from smaller k-point densities, as shown in Fig. S2b and c. We found that convergence with respect to k-point mesh was essential, as the BSE spectra required a much denser mesh than the PBE or G_0W_0 band gaps alone. In S2a we show the variation of the BSE (solid lines) and IPA (dashed lines) spectra of 2ML NPL with increasing k-point density, noting the qualitatively incorrect shape below a $10 \times 10 \times 1$ mesh. We note that a fully converged spectrum would require at least $25 \times 25 \times 1$ k-points; however, the exciton binding energy and near-quantitative comparison with experiment are obtained by $15 \times 15 \times 1$ k-points.

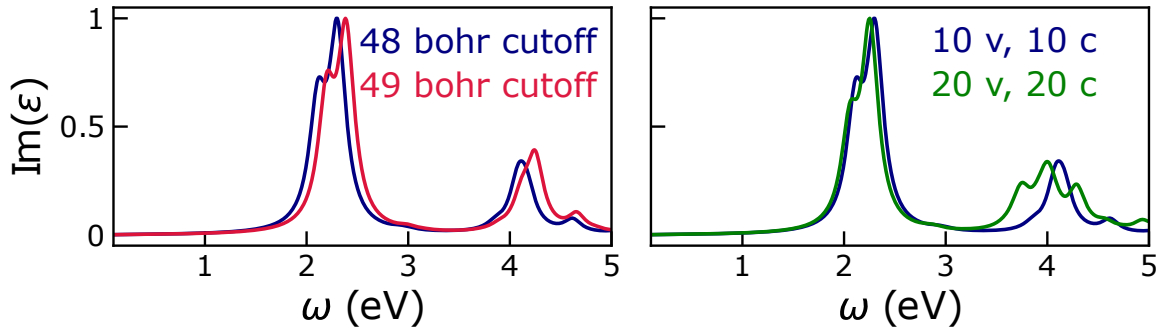


Figure S3: (left) $2 \times 2 \times 1$ k-point BSE spectrum for 2ML CdSe using a Coulomb cutoff set at 48 (blue) and 49 (red) Bohr. Total axial unit cell size is 49.4 Bohr. (right) $2 \times 2 \times 1$ k-point BSE spectrum for 2ML CdSe illustrating the difference between including 10 valence/10 conduction band states (blue) and 20 valence/20 conduction band states (green). v=valence band, c=conduction band.

Similarly to the Yambo G_0W_0 calculations, BSE calculations of 2D NPLs employed a Coulomb cutoff using the Random Integration Method (RIM) to converge with respect to vacuum size in the axial direction. The Yambo documentation recommends the Coulomb cutoff to be set approximately 1 Bohr smaller than the total unit cell size in the relevant direction. All BSE and G_0W_0 calculations adhered to this guideline, for example using a cutoff distance of 48.5 Bohr for the 2ML NPL, where the total axial unit cell size was 49.4 Bohr. Comparison of absorption spectra (using only $2 \times 2 \times 1$ k-point sampling) with a cutoff of 48 Bohr and 49 Bohr is shown in Fig. S3a in blue and red, respectively. As can be seen, the absorption spectra is quite insensitive to the cutoff value when it is close to the edge of

the unit cell; however, we found the spectra onset to vary substantially when the cutoff was reduced to near the center of the unit cell and lead to non-physical results.

The spectra presented in this work were calculated using transitions between 10 occupied and 10 unoccupied energy levels near the band edges to reduce the size of the matrices involved in the BSE calculation. We found this to be sufficient for the convergence of the first two absorption peaks (attributed to the light-hole and heavy-hole transitions), though more transitions would be required to fully converge the higher-energy regions of the spectra, as shown in Fig. S3.

Finally, the exciton binding energies calculated from BSE were compared to values predicted using the Screened 2D Hydrogen model of Olsen, *et al.*,¹¹ which uses a 2D polarizability as the fundamental variable to calculate the exciton binding energy. The in-plane 2D polarizability of the NPLs in this text was calculated using the self-consistent dielectric-dependent hybrid functional (sc-DDH),¹² as G_0W_0 calculations of this quantity were not computationally feasible and because we found PBE to strongly overestimate the polarizability values. In-plane polarizabilities were calculated in the Qbox code¹³ using finite differences. The in-plane polarizabilities (α) were then used to compute the effective dielectric constant (ε) entering the sc-DDH functional, as $\varepsilon = 1 + 4\pi\alpha/\Omega$. Here, we defined the effective volume (Ω) to be the area of the computational unit cell times an effective NPL thickness defined by the extents of the electrostatic potential (other definitions of volume based on the density and dielectric screening were tested as well, and a full discussion of the minor differences found adopting different definitions will be reported elsewhere). NPL effective masses were taken from tight-binding calculations by Benchamekh *et al.*,¹⁴ as we expect these values to be closest to the sc-DDH level of theory.

S2 Continuum elastic model for the detailed structure of core and core-shell nanoplatelets

We use a continuum elastic model to rationalize the in- and out-of-plane strain observed in our calculations. The model was previously proposed for thin metallic films,¹⁵ and includes surface stress to account for the presence of the surface.¹⁶ It accounts only for two exposed facets on the top and bottom of the NPL. Therefore, it assumes the NPL to be infinitely extended in the lateral direction. The in-plane direction is labeled as x , while the out-of-plane direction is defined as z .

There are two energies involved in “equilibrating”¹⁵ a thin film. The volume deformation energy of the bulk crystal (ΔU_{vol}), and work done against surface stress (ΔU_{s}). The overall work per unit surface, A_0 , is the normalized sum of the two:

$$\Delta\tilde{U} = \frac{\Delta U_{\text{vol}} + \Delta U_{\text{s}}}{A_0} = [L_{\text{NPL}}^0 Y_{\infty} \varepsilon_x^2 + \mathcal{O}(\varepsilon_x^3)] + 2f_0 (1 + \varepsilon_x)^2. \quad (\text{S1})$$

In Eq. S1, ε_x is the in-plane strain, L_{NPL}^0 is the NPL thickness in the absence of strain, and f_0 is the surface stress. The biaxial-modulus (Y_{∞}) in the 100-direction is defined for cubic crystals as $C_{11} + C_{12} - 2C_{12}^2/C_{11}$, where C_{ij} are the elastic constants.¹⁷ While f_0 has units of work per surface area, e.g. Nm^{-1} , the biaxial modulus has units of stress, e.g. Nm^{-2} . Note that for a state of biaxial stress, the out-of-plane strain (ε_z) is linked to the in-plane strain as $\varepsilon_z = -2C_{12}/C_{11}\varepsilon_x$.¹⁵

The in-plane strain of the equilibrated film ($\tilde{\varepsilon}_x$) is the one minimizing the overall work per unit surface, $\Delta\tilde{U}$. Ignoring terms larger than $\mathcal{O}(\varepsilon_x^2)$ in Eq. S1, the following expression for the equilibrium in-plane strain is obtained:

$$\tilde{\varepsilon}_x = \frac{-2f_0}{2f_0 + L_{\text{NPL}}^0 Y_{\infty}}. \quad (\text{S2})$$

Intuitively, Eq. S2 shows that the equilibrium in-plane strain decreases with increasing

NPL thickness, L_{NPL}^0 . For vanishing surface stress, the in-plane strain is zero.

S2.1 Model applied to core-shell heterostructures

Recent experimental advances have allowed for the synthesis of core-shell NPLs with c-ALD techniques, enabling the synthesis of core-shell heterostructures with monolayer precision.^{18,19} Due to the lattice-constant mismatch between the different layers of the heterostructure, one would expect layers with a smaller lattice constant to expand, while those with a larger lattice constant should contract in the in-plane direction. This induces an expansion (contraction) in the out-of-plane direction for layers with larger (smaller) in-plane lattice constants. However, atomically resolved electron microscopy images reveal an out-of-plane contraction of all layers in a NPL heterostructures.¹⁹ To rationalize this seemingly counterintuitive observation, we generalize the aforementioned continuum elastic model to also describe NPL heterostructures. First we discuss the case of a heterostructure with only one shell layer, e.g. simple core-shell NPLs. Then, we generalize the result to arbitrary core-shell heterostructures.

S2.1.1 Simple core-shell systems

For the case of a simple core-shell NPL—a core sandwiched between two shells of equal thickness—the volume deformation energy, ΔU_{vol} , in Eq. S1 needs to account for the deformation of both core $\Delta U_{\text{vol,c}}$ and shell $\Delta U_{\text{vol,sh}}$ materials. The surface energy term, ΔU_s , remains unchanged. Additionally, the equilibrium in-plane lattice constant of both materials needs to match, which constrains the in-plane strain of both core ($\tilde{\varepsilon}_{\text{c},x}$) and shell ($\tilde{\varepsilon}_{\text{sh},x}$) layers:

$$a_{\text{c},0} (1 + \tilde{\varepsilon}_{\text{c},x}) = a_{\text{sh},0} (1 + \tilde{\varepsilon}_{\text{sh},x}). \quad (\text{S3})$$

The lattice constants of the unstrained core and shell materials are $a_{\text{c},0}$ and $a_{\text{sh},0}$, respectively. Note that in- and out-of-plane strain are still linked by the elastic constants: $\tilde{\varepsilon}_{k,z} = -2C_{12}^k/C_{11}^k \tilde{\varepsilon}_{k,x}$ ($k = \text{c, sh}$). Using Eq. S3, we can write the volume deformation en-

ergy of the shell ($\Delta U_{\text{vol,sh}} = L_{\text{sh},0} Y_{\text{sh},\infty} \varepsilon_{\text{sh},x}^2$) as a function of the in-plane strain of the core ($\tilde{\varepsilon}_{c,x}$). The equilibrium in-plane strain of the core, $\tilde{\varepsilon}_{c,x}$, is the one minimizing the overall deformation energy per unit surface $\Delta\tilde{U} = (\Delta U_{\text{vol,c}} + \Delta U_{\text{vol,sh}} + \Delta U_s)/A_0$.

For a core of unstrained thickness $L_{c,0}$ sandwiched in between two shells of unstrained thickness $L_{\text{sh},0}$, the equilibrium in-plane strain of the core is given as

$$\tilde{\varepsilon}_{c,x} = \frac{-2f_0 - 2L_{\text{sh},0}Y_{\text{sh},\infty} \left[1 - \left(\frac{a_{\text{sh},0}}{a_{c,0}} \right) \right]}{2f_0 + 2L_{\text{sh},0}Y_{\text{sh},\infty} + L_{c,0}Y_{c,\infty}}. \quad (\text{S4})$$

In Eq. S4, $Y_{c,\infty}$ and $Y_{\text{sh},\infty}$ are the biaxial-moduli of the core and shell materials, and f_0 is the surface stress acting on the exposed facets of the heterostructure.

A close analysis of Eq. S4 reveals some interesting physical properties. Assuming the core material to have the greater lattice constant than the shell, which is the case for CdSe NPLs shelled with CdS, we immediately see that the numerator term in brackets remains positive. For vanishing surface stress, i.e. $f_0 = 0$, the equilibrium in-plane strain of the core is negative. The presence of surface stress, $f_0 > 0$, makes the equilibrium in-plane strain of the core even more negative. If the in-plane strain of the core is negative enough, e.g. for larger f_0 or for small $a_{\text{sh},0}/a_{c,0}$, the in-plane strain of the shell becomes negative too. This explains the overall in-plane contraction (or out-of-plane expansion) of all layers, reported in experiments for NPL heterostructures.

S2.1.2 Generalization to arbitrary core-shell heterostructures

For arbitrary core-shell heterostructures, the volume deformation energy in Eq. S1 needs to account for the deformation of all layers in the heterostructure, $\Delta U_{\text{vol}} = \sum_k \Delta U_{k,\text{vol}}$, where k runs over all layers. Similarly to the simple core-shell system, the surface energy term, ΔU_s , remains unchanged. By defining the i -th layer to be the reference layer, the lattice-matching condition then reads:

$$a_{i,0} (1 + \tilde{\varepsilon}_{i,x}) = a_{k,0} (1 + \tilde{\varepsilon}_{k,x}). \quad (\text{S5})$$

In Eq. S5, $a_{k,0}$ are the lattice constants of the unstrained layer materials. Using Eq. S5 we can write the in-plane strain of all layers, $\tilde{\varepsilon}_{k,x}$, as a function of the in-plane strain of the reference layer, $\tilde{\varepsilon}_{i,x}$:

$$\tilde{\varepsilon}_{k,x} = \gamma_{ik}(1 + \tilde{\varepsilon}_{i,x}) - 1; \quad \gamma_{ik} = \frac{a_{i,0}}{a_{k,0}}. \quad (\text{S6})$$

In each layer, in- and out-of-plane strain are connected through $\tilde{\varepsilon}_{k,z} = -2C_{12}^k/C_{11}^k \tilde{\varepsilon}_{k,x}$, where C_{ij}^k are the elastic constants of the k -th layer. Using the constraint from Eq. S5, together with the resulting dependence between $\tilde{\varepsilon}_{i,x}$ and $\tilde{\varepsilon}_{k,x}$ (Eq. S6), we obtain the equilibrium strain of the reference layer that minimizes the overall work per unit surface as:

$$\tilde{\varepsilon}_{i,x} = \frac{-2f_0 - \sum_k L_{k,0} Y_{k,\infty} (1 - \gamma_{ik}^{-1})}{2f_0 + \sum_k L_{k,0} Y_{k,\infty}}; \quad k = 1, \dots, N. \quad (\text{S7})$$

The biaxial-modulus for each layer is described by $Y_{k,\infty}$, while $L_{k,0}$ describes the unstrained thickness of each layer in the heterostructure. Note that when k equals i , γ_{ik} equals one and the second term in the numerator of Eq. S7 vanishes. Therefore, in the absence of any shell material — k equals i only — Eq. S7 simplifies to the expression of core-only NPLs, Eq. S2.

In summary, we have presented a continuum elastic model to describe the detailed structure of both core-only and core-shell NPLs. The model is simple, and therefore provides an intuitive understanding for what ultimately determines the structure of these systems. It also rationalizes observations which cannot be explained by the lattice-matching condition only: the presence of strain in core-only NPLs, and the overall in-plane contraction in core-shell heterostructures.

S3 Modelling the confinement energy

Models for charge-carrier confinement in NPLs need to account for the non-parabolicity of the conduction band (“electron dispersion”) in zincblende semiconductors,^{20,21} and also need

to include the effect of a finite potential-well confining the charge carriers^{22,23} (see Results and Discussion). For NPLs these two physical effects have so far been considered separately. Here we want to discuss a simple model that combines both.

To account for the non-parabolicity of the electron dispersion, we use an energy dependent, rather than constant, electron effective-mass $m_e(E)$ similar to Ref.:^{21,24–26}

$$m_e(E) = \left[\alpha + \frac{E_p}{3} \left(\frac{2}{E + E_g} + \frac{1}{E + E_g + \Delta} \right) \right]^{-1}, \quad (\text{S8})$$

where E_g is the bulk band gap, E_p is the Kane energy describing conduction- and valence-band mixing,²⁷ α describes the coupling between the conduction band (electron) to higher bands,^{20,21,24–26} and Δ is the energy splitting of the valence band due to spin-orbit coupling. The electron effective-mass at the bottom of the band is obtained for $E = 0$. Neglecting effects of non-parabolicity by assuming m_e as constant strongly affects the confinement energy, especially for thin NPLs.

We include the effect of a finite confining-potential (V_0) using a particle in a finite potential-well model (see e.g. Griffith²⁸). To account for the difference in electron and heavy-hole effective-mass inside (semiconductor layer) and outside (ligand and vacuum) the NPL, we apply continuity and current-conserving boundary conditions.²⁹ As a result, we obtain two implicit equations describing the confinement energy of the electron ($E_{e,\text{conf}}$) and heavy-hole ($E_{hh,\text{conf}}$):

$$\tan \left(\frac{L_{\text{NPL}}}{2} \sqrt{2m_e E_{e,\text{conf}}} \right) = \sqrt{m_e \left(\frac{V_0^e}{E_{e,\text{conf}}} - 1 \right)}; \quad (\text{S9})$$

$$\tan \left(\frac{L_{\text{NPL}}}{2} \sqrt{2m_{hh} E_{hh,\text{conf}}} \right) = \sqrt{m_{hh} \left(\frac{V_0^{hh}}{E_{hh,\text{conf}}} - 1 \right)}. \quad (\text{S10})$$

Note that Eq. S8-S10 (including the equations that follow) as well as the equations in the main text are given in atomic units. As done in models of quantum-dots²⁶ and NPLs,³⁰ a free-electron mass ($=1$ in a.u.) is assumed for heavy-hole and electron in the ligand shell

and the vacuum region surrounding the NPLs. The heavy-hole effective mass inside the NPL is given as $m_{\text{hh}} = (\gamma_1 - 2\gamma_2)^{-1}$, where γ_i are the modified Luttinger parameters of the bulk.²⁷ The electron effective-mass (m_e) is given as in Eq. S8 and depends on the electron confinement energy, $E_{\text{e,conf}}$. Note that the total confinement energy, E_{conf} , is the sum of $E_{\text{e,conf}}$ and $E_{\text{hh,conf}}$.

For better comparison with the result for core-shell systems (see next section) note that Eq. S9 and S10 can be re-written in compact form as:

$$\tan(k_0 z_1) = \gamma_{01}; \quad \gamma_{01} = \frac{m_0 k_1}{m_1 k_0} \quad (\text{S11})$$

where z_1 equals $L_{\text{NPL}}/2$, m_0 (m_1) is the effective-mass in semiconductor (ligand and vacuum layer). Further, k_0 is defined as $\sqrt{2m_0 E_{\text{conf}}}$. Similarly, k_1 equals $\sqrt{2m_1(V_1 - E_{\text{conf}})}$.

S3.1 Core-shell systems

For core-shell systems, we need to account for the presence of multiple confining potentials. Here, we discuss the case of a simple core shell system — a core sandwiched between two shells of equal thickness. The general case of arbitrary NPL heterostructures, not discussed here, is described by the transfer-matrix method.^{31,32}

For simple core-shell systems, we need to account for the confining potential due to the band offset between core and shell semiconductor materials (V_1), and the one due to the passivating ligands ($V_2 \geq V_1$). As displayed in Fig. S4a, the thickness of the core is $L_{\text{NPL}} = 2z_0$, while the shell thickness is z_1 . Given that we are interested in the quasiparticle gap of core-shell NPLs, we focus on the lowest confined state, confined only in the core $E_{\text{conf}} < V_1$. The wave function to the lowest-confined state is symmetric with respect to the out-of plane direction, $\Psi(z) = \Psi(-z)$. Then, the solutions to the Schrödinger equation in the core (region 0), shell (region 1), and ligand layer (region 3) for *positive* z are given as:

$$\Psi_0 = \cos(k_0 z); \quad k_0 = \sqrt{2m_0 E_{\text{conf}}}, \quad (\text{S12})$$

$$\Psi_1 = A_1 \exp(-k_1 z) + B_1 \frac{m_1}{k_1} \exp(k_1 z); \quad k_1 = \sqrt{2m_1(V_1 - E_{\text{conf}})}, \quad (\text{S13})$$

$$\Psi_2 = A_2 \exp(-k_2 z); \quad k_2 = \sqrt{2m_2(V_2 - E_{\text{conf}})}. \quad (\text{S14})$$

Note that the form of Eq. S12 and S14 is given by our assumption of a symmetric wave function, $\Psi(z) = \Psi(-z)$, and the requirement that $\Psi(z)$ vanishes as z approaches infinity. For the wave function in the shell region, Ψ_1 , we used the specific form proposed by Pavese *et al.*,³² as it simplifies the derivation.

There are three normalization constants that are yet to be determined in Eq. S12-S14. Imposing continuity and current-conserving boundary conditions²⁹ in z_0 and z_1 , provides four constraints on the wave functions:

$$\Psi_0(z_1) = \Psi_1(z_1); \quad \left. \frac{1}{m_0} \frac{d\Psi_0}{dz} \right|_{z_1} = \left. \frac{1}{m_1} \frac{d\Psi_1}{dz} \right|_{z_1}, \quad (\text{S15})$$

$$\Psi_1(z_2) = \Psi_2(z_2); \quad \left. \frac{1}{m_1} \frac{d\Psi_1}{dz} \right|_{z_2} = \left. \frac{1}{m_2} \frac{d\Psi_2}{dz} \right|_{z_2}. \quad (\text{S16})$$

The boundary conditions at z_2 link A_1 and B_1 to A_2 :

$$A_1 = \frac{A_2}{2} e^{(k_1 - k_2)z_2} (1 + \gamma_{12}), \quad (\text{S17})$$

$$B_1 = \frac{A_2 k_1}{2m_1} e^{-(k_1 + k_2)z_2} (1 - \gamma_{12}), \quad (\text{S18})$$

where γ_{12} equals $(m_1 k_2)/(m_2 k_1)$. By inserting Eq. S17 and S18 into the continuity and current-conserving boundary condition at z_1 (Eq. S15) we obtain:

$$\cos(k_0 z_1) = \frac{A_2 e^{-k_2 z_1}}{2} [(1 + \gamma_{12})e^{k_1 d_1} + (1 - \gamma_{12})e^{-k_1 d_1}], \quad (\text{S19})$$

$$\sin(k_0 z_1) = \frac{A_2 e^{-k_2 z_1}}{2} \gamma_{01} [(1 + \gamma_{12})e^{k_1 d_1} - (1 - \gamma_{12})e^{-k_1 d_1}], \quad (\text{S20})$$

where γ_{ij} equals $(m_i k_j)/(m_j k_i)$. In Eq. S19 and S20, d_1 is the shell thickness, $d_1 = z_2 - z_1$. Dividing Eq. S20 by Eq. S19 eliminates the dependence on A_2 and provides an implicit equation for all k_i :

$$\tan(k_0 z_1) = \gamma_{01} \frac{\tanh(k_1 d_1) + \gamma_{12}}{1 + \gamma_{12} \tanh(k_1 d_1)} \quad (\text{S21})$$

Since all k_i depend on E_{conf} , Eq. S21 provides an implicit equation for the confinement energy in a core-shell NPL.

The expression given in Eq. S21 displays two limiting cases that have a straightforward physical interpretation: when d_1 vanishes, V_2 dominates and we recover the single finite potential well solution $\tan(k_0 z_1) = \gamma_{02}$ (note that $\gamma_{01}\gamma_{12} = \gamma_{02}$). The opposite is true when d_1 approaches infinity: we recover the single-well solution with confining potential V_1 — $\tan(k_0 z_1) = \gamma_{01}$.

Similarly to core-only systems we emphasize two important points. When describing the confinement of holes, effective masses can be assumed to be independent of E_{conf} in all three regions. This is different in the case of electrons, where the dispersion is non-parabolic. In this case, the effective mass of the electron in the core-region, m_0 , depends on E_{conf} , and is described by Eq. S8. This dependence on E_{conf} must be accounted for when solving Eq. S21.

S4 Model of quasiparticle gap applied to core-shell NPLs: the case of a CdSe core and CdS shell

We apply the model for the quasiparticle gap, discussed in the main text for core-only NPLs, to core-shell systems. Specifically, to the case of a CdSe core shelled by CdS. The

fundamental quasiparticle gap, $E_{\text{NPL}}^{\text{QP}}$, for core-shell NPLs can still be estimated as:

$$E_{\text{NPL}}^{\text{QP}} = E_{\text{QP,bulk}} + \Delta E_{\text{strain}}^{\text{bulk}} + E_{\text{conf}} + E_{\text{self}}. \quad (\text{S22})$$

While $E_{\text{QP,bulk}}$ still corresponds to the bulk band gap of the core (CdSe), $\Delta E_{\text{strain}}^{\text{bulk}}$, E_{conf} , and E_{self} strongly depend on the presence of a shell.

The shell thickness determines the amount of in- and out-of-plane strain in the core, which affects $\Delta E_{\text{strain}}^{\text{bulk}}$. To account for this, we compute the strain-profile in the core as a function of shell thickness using the continuum elastic model (Eq. S4). As input parameters to the model, we use elastic properties and lattice constants of core and shell materials from literature.³³ The value for the surface stress ($f_0 = 0.321 \text{ N/m}$) is extracted directly from our simulations of chloride-passivated core-only NPLs, so that Eq. S2 fits the first principles data. Results are plotted in Fig. S4b showing the out-of-plane strain as a function of CdS shell thickness, and for CdSe cores of different thickness. Results for core-only NPLs correspond to a shell thickness of zero. As expected, independent of NPL core thickness, adding a CdS leads to additional in-plane contraction and, consequently, out-of-plane expansion. This is because CdS exhibits a smaller lattice constant than CdSe. Increasing the thickness of the CdSe core decreases the out-of-plane strain.

The strain profile—calculated using the continuum elastic model—is then used to compute the change in band gap due to strain ($\Delta E_{\text{strain}}^{\text{bulk}}$). This is done using Eq. 3 from the main text. For cores of different thicknesses, Fig. S4c displays the change in band gap due to strain, $\Delta E_{\text{strain}}^{\text{bulk}}$, as a function of shell thickness. The deformation potentials needed to compute $\Delta E_{\text{strain}}^{\text{bulk}}$ were extracted to fit PBE calculations of strained bulk ($a_p = -15.84 \text{ eV}$, $a = 14.17 \text{ eV}$, and $b = -1.05 \text{ eV}$).

Next, we discuss how the shell affects changes in band gap due to the dielectric environment (E_{self}). CdS and CdSe have similar dielectric constants compared to the environment. By assuming them to be the same we can use the expression by Cho *et al.*³⁴ (Eq. 5 from

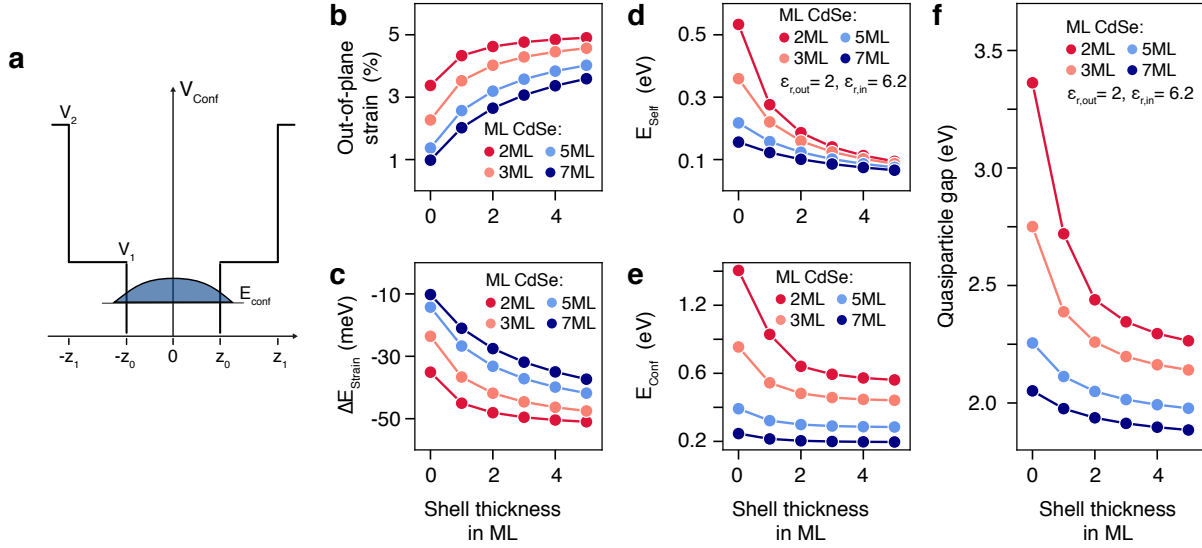


Figure S4: (a) Confining potentials in a core-shell NPLs. The confined wave function of the lowest confined state is drawn schematically. Strain-profile (b) and different energy contributions (c-e) to the quasiparticle gap (see Eq. S22) plotted as a function of shell thickness, for CdSe cores of different thicknesses. (d) quasiparticle gap of core-shell NPLs computed using the model of Eq. S22, and plotted as a function of shell thickness for different cores.

the main text) to estimate E_{self} in core-shell NPLs. Note that the thickness entering their model is no longer the thickness of the core only, but also includes the shell. In Fig. S4d we plot E_{self} as a function of core and shell thickness. Results are computed assuming $\epsilon_{r,\text{out}} = 2$. They show that increasing the number of shells decreases E_{self} . In the limit of infinitely thick shells, E_{self} vanishes.

Finally, we study how the presence of a shell changes the confinement of charge carriers. Band-parameters entering the model of Eq. S21 (effective-masses) were taken from Ithurria *et al.*²⁰ Only the effective-mass of the electron in the CdSe core was assumed to depend on the confinement energy (Eq. S8). In the CdS shell, where $E_{\text{e,conf}} < V_1$, the effective mass was assumed to be constant, $m_{\text{e,CdS}} = 0.196$ a.u.²⁰ Similar to the main text, we assume a free-electron mass in the ligand and vacuum region. The band offsets that determine the confinement potential between core and shell (V_1) were taken from Llusar *et al.*²³ For simplicity, we have neglected strain-effects on the confinement potential (V_1). However, if

needed, they can be easily incorporated within our model. The confinement potential due to the passivating ligands (V_2) was assumed to be 2.5 eV, as in the main text.

In Fig. S4d we plot the confinement energy, computed using Eq. S21, as a function of shell thickness and for NPL cores of different thicknesses. Results for core-only NPLs are also displayed (0 ML). Our results show that the confinement energy already saturates when the shell is 5ML thick. This is in line with the two limiting cases discussed above and in the main text: the confinement energy is (i) highest for core-only ($V_2 > V_1$) where confinement is dictated by the ligands(V_2), and (ii) smallest for thick shells, where the contribution from the ligands (V_2) vanishes.

The quasiparticle gap of core-shell NPLs depends on all aforementioned physical effects (see Eq. S22). The quasiparticle gap is plotted in Fig. S4f as a function of shell thickness and for CdSe cores of different thicknesses. The results show that most shifts in quasiparticle gap due to the shell occur when the first few shell-layers are added. This is in qualitative agreement with experimental reports on the optical gap of core-shell NPLs.^{19,35} Analyzing the different contributions of $\Delta E_{\text{strain}}^{\text{bulk}}$, E_{conf} , and E_{self} to the shift in quasiparticle gap (Fig. S4c-e) reveals; the shift is mainly determined by the presence of a reduced confining potential of the shell material compared to the ligands ($V_2 > V_1$), and a reduced dielectric mismatch, due to the similar dielectric constant of core and shell.

References

- (1) Szemjonov, A.; Pauporté, T.; Ithurria, S.; Lequeux, N.; Dubertret, B.; Ciofini, I.; Labat, F. Ligand-Stabilized CdSe Nanoplatelet Hybrid Structures with Tailored Geometric and Electronic Properties. New Insights from Theory. *RSC Adv.* **2014**, *4*, 55980–55989.
- (2) van Setten, M. J.; Giantomassi, M.; Bousquet, E.; Verstraete, M. J.; Hamann, D. R.; Gonze, X.; Rignanese, G.-M. The PseudoDojo: Training and Grading a 85 Element

- Optimized Norm-Conserving Pseudopotential Table. *Comput. Phys. Commun.* **2018**, *226*, 39–54.
- (3) Govoni, M.; Galli, G. Large Scale GW Calculations. *J. Chem. Theory Comput.* **2015**, *11*, 2680–2696.
- (4) Smart, T. J.; Wu, F.; Govoni, M.; Ping, Y. Fundamental Principles for Calculating Charged Defect Ionization Energies in Ultrathin Two-Dimensional Materials. *Phys. Rev. Mater.* **2018**, *2*, 124002.
- (5) Sangalli, D.; Ferretti, A.; Miranda, H.; Attaccalite, C.; Marri, I.; Cannuccia, E.; Melo, P. M.; Marsili, M.; Paleari, F.; Marrazzo, A. et al. Many-Body Perturbation Theory Calculations Using the Yambo Code. *J. Phys. Condens. Matter* **2019**, *31*, 325902.
- (6) Marini, A.; Hogan, C.; Grüning, M.; Varsano, D. Yambo: An Ab Initio Tool for Excited State Calculations. *Comput. Phys. Commun.* **2009**, *180*, 1392–1403.
- (7) Godby, R. W.; Needs, R. J. Metal-Insulator Transition in Kohn-Sham Theory and Quasiparticle Theory. *Phys. Rev. Lett.* **1989**, *62*, 1169–1172.
- (8) Engel, G. E.; Farid, B. Generalized Plasmon-Pole Model and Plasmon Band Structures of Crystals. *Phys. Rev. B* **1993**, *47*, 15931–15934.
- (9) Stankovski, M.; Antonius, G.; Waroquiers, D.; Miglio, A.; Dixit, H.; Sankaran, K.; Giantomassi, M.; Gonze, X.; Côte, M.; Rignanese, G.-M. G^0W^0 Band Gap of ZnO: Effects of Plasmon-Pole Models. *Phys. Rev. B* **2011**, *84*, 241201.
- (10) Morokoff, W. J.; Caffisch, R. E. Quasi-Monte Carlo Integration. *J. Comput. Phys.* **1995**, *122*, 218–230.
- (11) Olsen, T.; Latini, S.; Rasmussen, F.; Thygesen, K. S. Simple Screened Hydrogen Model of Excitons in Two-Dimensional Materials. *Phys. Rev. Lett.* **2016**, *116*, 056401.

- (12) Skone, J. H.; Govoni, M.; Galli, G. Self-Consistent Hybrid Functional for Condensed Systems. *Phys. Rev. B* **2014**, *89*, 195112.
- (13) Gygi, F. Architecture of Qbox: A Scalable First-Principles Molecular Dynamics Code. *IBM J. Res. Dev.* **2008**, *52*, 137–144.
- (14) Benchamekh, R.; Gippius, N. A.; Even, J.; Nestoklon, M.; Jancu, J.-M.; Ithurria, S.; Dubertret, B.; Efros, Al. L.; Voisin, P. Tight-Binding Calculations of Image-Charge Effects in Colloidal Nanoscale Platelets of Cdse. *Phys. Rev. B* **2014**, *89*, 035307.
- (15) Streitz, F. H.; Cammarata, R. C.; Sieradzki, K. Surface-Stress Effects on Elastic Properties. I. Thin Metal Films. *Phys. Rev. B* **1994**, *49*, 10699.
- (16) Gurtin, M. E.; Murdoch, A. I. Surface Stress in Solids. *Int. J. Solids Struct.* **1978**, *14*, 431–440.
- (17) Knowles, K. M. The biaxial moduli of cubic materials subjected to an equi-biaxial elastic strain. *J. Elast.* **2016**, *124*, 1–25.
- (18) Ithurria, S.; Talapin, D. V. Colloidal Atomic Layer Deposition (c-ALD) using Self-Limiting Reactions at Nanocrystal Surface Coupled to Phase Transfer between Polar and Nonpolar Media. *J. Am. Chem. Soc.* **2012**, *134*, 18585–18590.
- (19) Hazarika, A.; Fedin, I.; Hong, L.; Guo, J.; Srivastava, V.; Cho, W.; Coropceanu, I.; Portner, J.; Diroll, B. T.; Philbin, J. P. et al. Colloidal Atomic Layer Deposition with Stationary Reactant Phases Enables Precise Synthesis of “Digital” II–VI Nano-Heterostructures with Exquisite Control of Confinement and Strain. *J. Am. Chem. Soc.* **2019**, *141*, 13487–13496.
- (20) Ithurria, S.; Tessier, M.; Mahler, B.; Lobo, R.; Dubertret, B.; Efros, Al. L. Colloidal Nanoplatelets with Two-Dimensional Electronic Structure. *Nat. Mater* **2011**, *10*, 936–941.

- (21) Ji, B.; Rabani, E.; Efros, Al. L.; Vaxenburg, R.; Ashkenazi, O.; Azulay, D.; Banin, U.; Millo, O. Dielectric Confinement and Excitonic Effects in Two-Dimensional Nanoplatelets. *ACS Nano* **2020**, *14*, 8257–8265.
- (22) Christodoulou, S.; Climente, J. I.; Planelles, J.; Brescia, R.; Prato, M.; Martín-García, B.; Khan, A. H.; Moreels, I. Chloride-Induced Thickness Control in CdSe Nanoplatelets. *Nano Lett.* **2018**, *18*, 6248–6254.
- (23) Llusar, J.; Planelles, J.; Climente, J. I. Strain in Lattice-Mismatched CdSe-Based Core/Shell Nanoplatelets. *J. Phys. Chem. C* **2019**, *123*, 21299–21306.
- (24) Wetzel, C.; Efros, Al. L.; Moll, A.; Meyer, B.; Omling, P.; Sobkowicz, P. Dependence on Quantum Confinement of the In-Plane Effective Mass in $\text{Ga}_{0.47}\text{In}_{0.53}\text{As}/\text{InP}$ Quantum Wells. *Phys. Rev. B* **1992**, *45*, 14052.
- (25) Ekimov, A. I.; Hache, F.; Schanne-Klein, M. a.; Ricard, D.; Flytzanis, C.; Kudryavtsev, I.; Yazeva, T.; Rodina, A.; Efros, Al. L. Absorption and Intensity-Dependent Photoluminescence Measurements on CdSe Quantum Dots: Assignment of the First Electronic Transitions. *J. Opt. Soc. Am. B* **1993**, *10*, 100–107.
- (26) Norris, D. J.; Bawendi, M. Measurement and Assignment of the Size-Dependent Optical Spectrum in CdSe Quantum Dots. *Phys. Rev. B* **1996**, *53*, 16338.
- (27) Bahder, T. B. Eight-Band k·p Model of Strained Zinc-Blende Crystals. *Phys. Rev. B* **1990**, *41*, 11992.
- (28) Griffiths, D. J. *Introduction to Quantum Mechanics*, 2nd ed.; Pearson, 2005; pp 78–80.
- (29) Yu, P. Y.; Cardona, M. *Fundamentals of Semiconductors*, 3rd ed.; Springer: Berlin, 2001; pp 479–488.
- (30) Zelewski, S. J.; Nawrot, K. C.; Zak, A.; Gladysiewicz, M.; Nyk, M.; Kudrawiec, R. Exciton Binding Energy of Two-Dimensional Highly Luminescent Colloidal Nanostruc-

- tures Determined from Combined Optical and Photoacoustic Spectroscopies. *J. Phys. Chem. Lett.* **2019**, *10*, 3459–3464.
- (31) Jonsson, B.; Eng, S. T. Solving the Schrodinger Equation in Arbitrary Quantum-Well Potential Profiles Using the Transfer Matrix Method. *IEEE J. Quantum Electron.* **1990**, *26*, 2025–2035.
- (32) Pavesi, L.; Reinhart, F. Transfer Matrix Method to Compute Energy Levels of Superlattices. *Phys. Status Solidi B* **1990**, *157*, 615–626.
- (33) Ouendadji, S.; Ghemid, S.; Meradji, H.; Hassan, F. E. H. Theoretical Study of Structural, Electronic, and Thermal Properties of CdS, CdSe and CdTe Compounds. *Comput. Mater. Sci.* **2011**, *50*, 1460–1466.
- (34) Cho, Y.; Berkelbach, T. C. Environmentally Sensitive Theory of Electronic and Optical Transitions in Atomically Thin Semiconductors. *Phys. Rev. B* **2018**, *97*, 041409.
- (35) Rossinelli, A. A.; Riedinger, A.; Marqués-Gallego, P.; Knüsel, P. N.; Antolinez, F. V.; Norris, D. J. High-Temperature Growth of Thick-Shell CdSe/CdS Core/Shell Nanoplatelets. *ChemComm* **2017**, *53*, 9938–9941.